IEEE Photonics Journal
An IEEE Photonics Society Publication

Open Access

Design of an Athermal Interferometer Based on Tailored Subwavelength Metamaterials for On-Chip Microspectrometry

Volume 11, Number 6, December 2019

Umair A. Korai, *Student Member, IEEE*
Alaine H. Bermello
Michael J. Strain, *Member, IEEE*
Ivan Glesk, *Senior Member, IEEE*
Aitor V. Velasco

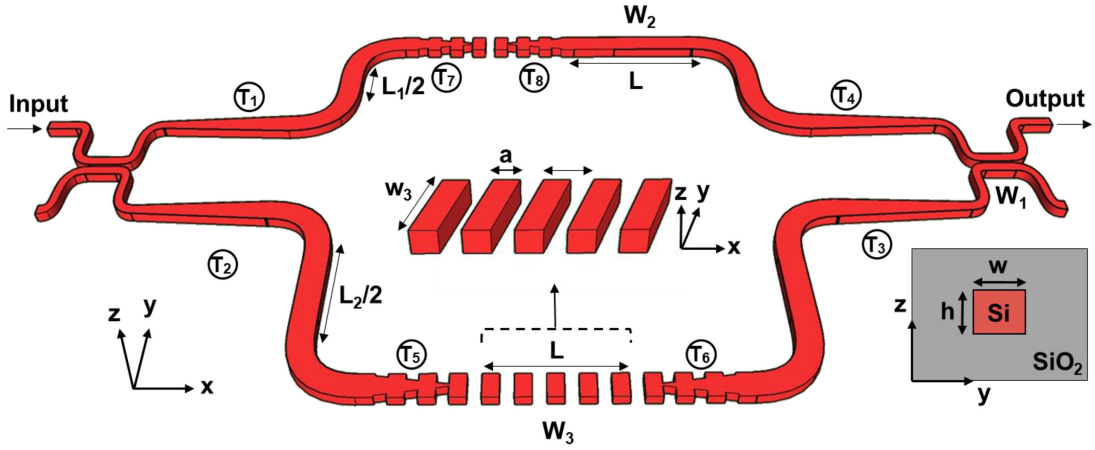

DOI: 10.1109/JPHOT.2019.2943774

Design of an Athermal Interferometer Based on Tailored Subwavelength Metamaterials for On-Chip Microspectrometry

Umair A. Korai,[1] ***Student Member, IEEE***, **Alaine H. Bermello**,[2] **Michael J. Strain**,[3] ***Member, IEEE***, **Ivan Glesk**,[1] ***Senior Member, IEEE***, **and Aitor V. Velasco** [2]

[1]Department of Electronic and Electrical Engineering, University of Strathclyde, Glasgow G1 1XW, U.K.
[2]Institute of Optics, Spanish National Research Council, Madrid 28006, Spain
[3]Institute of Photonics, Department of Physics, University of Strathclyde, Glasgow G1 1RD, U.K.

DOI:10.1109/JPHOT.2019.2943774

Manuscript received August 12, 2019; revised September 18, 2019; accepted September 21, 2019. Date of publication September 25, 2019; date of current version October 30, 2019. This work was supported in part by the Commonwealth Scholarship Commission, United Kingdom; Department of Telecommunication Engineering, Mehran University of Engineering and Technology, Jamshoro, 76062, Pakistan, in part by the European Union Horizon 2020 research and innovation program under the Marie Skłodowska-Curie under Grant 734331, in part by the Spanish Ministry of Science, Innovation and Universities under Grants RTI2018-097957-B-C33 and IJCI-2016-30484, and in part by the Community of Madrid - FEDER funds under Grant SINFOTON2-CM S2018/NMT-4326. Corresponding author: Umair A. Korai (e-mail: Umair.korai@strath.ac.uk).

Abstract: Temperature dependence is one of the main challenges of the silicon-on-insulator platform due to the large thermo-optic coefficient of its core material. In this work we propose a design of an all-passive athermal silicon-on-insulator Mach-Zehnder interferometer (MZI) based on the standard silicon material platform. The MZI's temperature compensation is achieved by optimizing the relative length of the wire and subwavelength grating arms and by tailoring the thermal response of the subwavelength structure. Simulations of the device performance showed that an overall temperature sensitivity of 7.5 pm/K could be achieved over a 100 nm spectral range near the 1550 nm region.

Index Terms: Integrated optics, athermal design, spectroscopy, thermo-optic effects, silicon-on-insulator.

1. Introduction

On-chip Fourier-transform (FT) microspectrometers have shown remarkable potential in the field of integrated spectroscopy [1], [2]. They offer an improved signal-to-noise ratio (SNR) and optical throughput (*étendue*) over traditional Fourier-transform (FT) systems [3], while circumventing the need for moving or active elements [4]. Unlike other types of microspectrometers such as Bragg, concave [5], [6], and arrayed waveguide gratings (AWG) [7] or cascaded microring resonators [8], on-chip FT microspectrometers offer multiple-aperture schemes and an independent channel calibration. The integrated FT spectrometer can be implemented through an array of waveguide based Mach-Zehnder interferometers (MZI) with linearly increasing optical path differences (OPD)

[9], [10]. In addition, the silicon-on-insulator (SOI) high mode confinement, enabled by the high refractive index of silicon (3.47 at 1550 nm), [11] and the availability of optical delays, has enabled high resolution and compact footprints [1], [12]. Although these techniques were originally developed for the C-band (1.529–1.56 μm), the versatility and advantages of this configuration has led to their extension into other wavelength ranges, namely the mid-infrared (3–8 μm) [13], with notable applications in absorption sensing.

However, the operation of the FT microspectrometer has some technological challenges. Fabrication errors, especially deviations from waveguide nominal widths, will produce arbitrary variations in the effective refractive index of silicon waveguides and therefore the OPD and transfer function of each MZI. Such variations introduce phase errors in the interferogram which limits the spectral resolution of the devices. These type of errors can be avoided by implementing heaters [14] or fully passive spectral retrieval techniques [1], [15]. Both methods require maintaining stable environmental conditions between the time of calibration and operation. Due to the high thermal dependence of silicon waveguides (1.8×10^{-4} K^{-1} and 1.2×10^{-4} K^{-1} at 1.55 μm for the TE and TM polarization, respectively) [16] even small temperature variations will produce significant phase errors. This imposes very demanding thermal stability requirements and limits the device applicability and performance. Software techniques relying on a temperature-sensitive calibration [17] have been developed to improve the resolution down to 17 pm. However, hardware athermalization of Mach-Zehnder interferometers can also be used for further resolution enhancements. Several methods have been proposed for a design of a temperature insensitive MZIs and ring resonators [18]–[24]. The most common approach is to use a polymer as the cladding material due to its negative thermo-optic coefficient [18], [19]. This solution is limited by the polymer dependence on changing environment conditions such as the moisture or mechanical pressure. Titanium oxide (TiO_2) [20], [21] or a combination of TiO_2 and silicon nitride (Si_3N_4) [22] have been also proposed as cladding alternatives. However, for any given material platform, thermal independence can also be achieved by combining waveguide segments of different geometries and thermal response. In particular, by introducing temperature compensating segments as wider or narrower waveguides in one of the interferometer arms and adequately designing their relative lengths, the overall MZI thermal response can be compensated [23], [24]. This opens a promising path for a FT athermalization. A broadband thermo-optic compensation and resilience to fabrication deviations from a nominal design are still required.

Subwavelength gratings with a polymer cladding have already been proposed for use in athermal waveguide designs [25], [26]. Subwavelength gratings (SWG) [27] are alternating sections of core and cladding materials periodically arranged with a period much smaller than the wavelength of the propagating light. Diffractive and Bragg effects are therefore suppressed and the approach effectively generates an optical metamaterial behaving as a homogeneous medium. The effective refractive index and dispersive properties of SWG structures can be tailored by modifying the grating period (Λ) and its duty cycle (DC) [28]. This enables the design of broadband devices such as couplers [29], multimode interference (MMIs) [30] or mode multiplexers [31], to name a few. SWG gratings can also enable the reduction of birefringence in silicon waveguide devices [32], [33]. Because the thermo-optic response of the SWG waveguide (compare to conventional wire waveguides) strongly depends on the thermo-optic coefficient of the cladding material, it is the basis for polymer-based athermal solutions [25], [26] in the aforementioned compensation of the thermo-optic effect in passive silicon photonics platforms.

In this paper, we present an athermal MZI with a tailored SWG waveguide. The use of a SWG circumvents the need for polymer claddings. It also adds an extra degree of design freedom for controlling the SWG effective refractive index and dispersion through adjusting the SWG duty cycle and dimensions which increases the bandwidth of the athermal MZI, compared to a width based solution [23], [24]. The proposed MZI design achieved the minimal overall temperature sensitivity, i.e., $\pm$4 pm/K. This was obtained for a 75 mm long MZI in a 100 nm wavelength rage around 1550 nm and is insensitive to length variation up to $\pm$0.355 mm.

This manuscript is organized as follows: Section 2 describes the operational principle of the proposed athermal MZI and gives modeling details. Section 3 presents the design of an athermal MZI

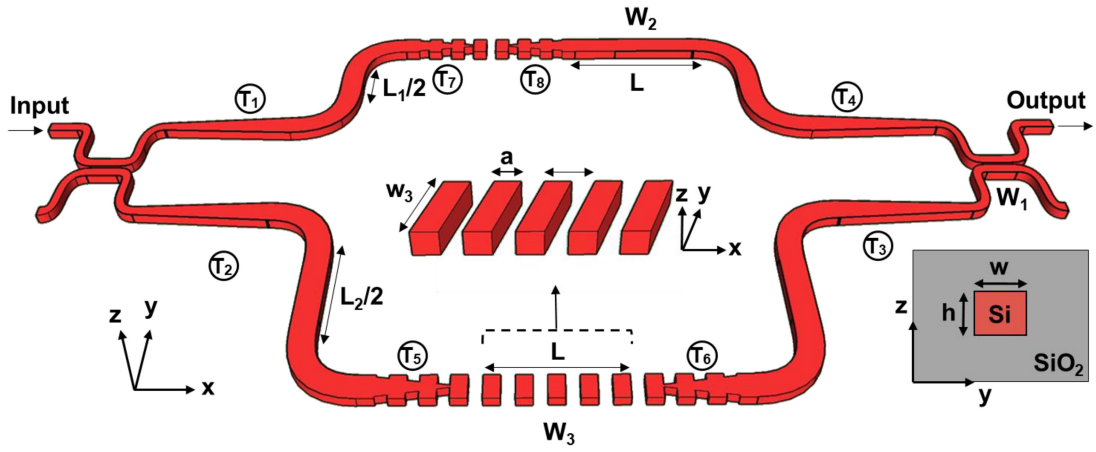

Fig. 1. Schematic diagram of the proposed athermal interferometer based on tailored subwavelength metamaterials. The central inset shows in detail the schematic of the subwavelength waveguide (lower arm), whereas the corner inset presents the geometry of the wire waveguide (upper arm).

and its performance simulations. The design leading to resilience to fabrication errors is presented in Section 4. Solutions for bandwidth enhancements are discussed in Section 5 and conclusions are presented in Section 6.

2. Operation Principle

A schematic structure of the proposed athermal MZI is shown in Fig. 1, where two differently structured MZI arms based on wire and SWG waveguides are coupled using two 50:50 directional couplers. In the upper arm, only a wire waveguide is used, whereas in the lower arm a combination of both, wire waveguide and SWG waveguide, is implemented. Modes propagating in each arm of the MZI will experience a corresponding change of the effective refractive index ($\frac{dn_{eff}}{dT}$) due to temperature fluctuations. Since the effective index of a waveguide also depends on its width and height [11] (in our design the height is kept constant and equal to 220 nm), by appropriately choosing the width and length of both arms of the MZI, the total change in $\frac{dn_{eff}}{dT}$ of the upper arm can be compensated by the total change in $\frac{dn_{eff}}{dT}$ of the lower arm. Thus, the overall temperature sensitivity of the MZI (at the targeted operational wavelength) can be brought to zero. In order to understand the above concept, we decompose the MZI arms into two sections:

The first section is a *delay section* common to both arms and uses the same waveguide geometry (therefore has the same effective refractive index and thermo-optic response) but has a different length L_1 in the upper arm and L_2 in the lower arm. The second section is the thermal compensating section. This section has the same length L in both arms but different structures: the wire waveguide is used in the upper arm and SWG in the lower arm.

In order to optimize the MZI's athermal design, we have considered the following waveguides and associated widths (see Fig. 1). The MZI input and output waveguides have a fixed width (W_1). The wire and SWG waveguides of the MZI arms have widths W_2 and W_3, which are optimized as described in Section 3. Four trapezoidal tapers (T_1 – T_4) [34] (two per arm), each having a length of 120 μm [35], are used to adiabatically adapt the mode size from the narrower input/output waveguide (width W_1) into the MZI wire waveguide (width W_2). Since the dimensions of the tapers are the same in both arms, the overall temperature sensitivity due to the presence of T_1 and T_4 in the upper arm is cancelled with the overall temperature sensitivity of T_2 and T_3 in the lower arm. SWG tapers (T_5 – T_6) are included in the lower arm of the MZI to minimize the transitions loss between wire and SWG waveguides. Details on SWG taper geometry can be found in [27], producing an adiabatic mode conversion in a taper length of 50 μm. Since the presence of these SWG tapers would affect the overall MZI thermal response, two identical back-to-back tapers

(T_7 – T_8) were included in the upper arm. Therefore, any thermally induced phase shift on tapers T5 and T6 is balanced by the presence of the same change on tapers (T_7 and T_8).

The response of the described athermal MZI is then given as:

$$m\lambda_0 = n_{eff_2} \cdot \Delta L + \Delta n_{eff} \cdot L \tag{1}$$

where n_{eff_2} is an effective index of the MZI wire waveguide; $\Delta L = L_2 - L_1$ is the physical length difference between both MZI arms; $\Delta n_{eff} = n_{eff_3} - n_{eff_2}$ is the effective index difference between SWG and wire waveguides; and m is a parameter that, if an integer, indicates the order of a constructive interference at the wavelength λ_0, and if a half integer, will result in a destructive interference. When considering the waveguides dispersion, the interference order (M) of the MZI can be written as [23], [24]:

$$M = m - \Delta L \frac{dn_{eff_2}}{d\lambda} - L \frac{d\left(\Delta n_{eff}\right)}{d\lambda} \tag{2}$$

The free spectral range (FSR) of an athermal MZI is defined by [23], [24]:

$$\lambda_{FSR} = \frac{\lambda_0}{M} \tag{3}$$

and the overall temperature sensitivity (S) of this athermal MZI at any specified wavelength (λ_0) is given as [23], [24]:

$$S = \frac{\Delta\lambda 0}{\Delta T} = \frac{\Delta L \frac{dn_{eff_2}}{dT} + L \frac{d\Delta n_{eff}}{dT}}{M}. \tag{4}$$

Because silicon has a positive thermo-optic coefficient, the first term of (4) is always positive. The term $\frac{d\Delta n_{eff}}{dT}$ in (4) can be negative by choosing parameters of the wire and SWG waveguide such that the effective index of the SWG waveguide (n_{eff_3}) is lower than the effective index of the wire waveguide (n_{eff_2}). Therefore, by appropriately choosing the width and duty cycle of the SWG waveguide, then adequately selecting the length of each waveguide section, the overall thermal response of the MZI can be annulled for the targeted central wavelength (λ_0).

In order to evaluate the performance of the athermal MZI, two parameters were defined: a relative optical path difference (r_{OPD}) and total temperature sensitivity (S_{total}):

r_{OPD} is given by (5). It relates the physical length of the MZI's longest arm to the optical path difference attained when the athermal condition is met. That is, higher r_{OPD} values will result in a more compact device with the target OPD value. In other words, for a fixed OPD value, the shorter the total length of a device, the higher its r_{OPD} value will be. This means, more compact spectrometers with a desired resolution can be designed and fabricated:

$$r_{OPD} = \frac{OPD}{L_1 + L_2 + 2L} \tag{5}$$

S_{total} is given by (6). It helps to evaluate the MZI athermalization bandwidth by determining variations of S for a given wavelength range (λ_{min}, λ_{max}):

$$S_{total} = S_{max} - S_{min} \tag{6}$$

where S_{max} and S_{min} is the maximum and minimum temperature sensitivity within the aforementioned wavelength range.

Finally, to ensure we can compare obtained results with those in [23], we define a length variation (δL) as a maximum allowed deviation from a 'common' length L (see Fig. 1) that preserves the value of S within a $\pm$1 pm/K range (at the central wavelength).

3. MZI Athermal Design

In this section, we present the optimization of the MZI and its SWG geometrical parameters in order to achieve the best device performance in terms of r_{OPD} and S_{total} for a standard SOI platform

with a silicon cladding. The effective index computations of the SWG waveguide Bloch modes were carried out using a commercial Finite Difference Time Domain (FDTD) simulation tool (Lumerical) [36], considering a TE polarization and a central wavelength 1550 nm in all cases. The effective index of the SWG waveguides was computed through Floquet-Bloch analysis [37], taking into account material dispersion properties. In our 3-D simulations, we have considered a 220-nm-thick silicon platform surrounded by a 2-μm-thick silica (SiO2) upper cladding and buried oxide (BOX) layer. The refractive index of Si and SiO2 in our 3-D FDTD simulation model are considered as 3.47 and 1.44, respectively, at the central wavelength of 1550 nm. The effective refractive index of SWG waveguides was also verified through band structure computations [38], resulting in an effective refractive index of 1.63 for W3 = 500 nm and DC = 50% at central wavelength of 1550 nm. A detailed mesh comprising of more than 40 data points per grating period was considered for accurate calculations. Effects of temperature changes on the effective index of the SWG and wire waveguide were calculated by considering a thermo-optic coefficient of Si as $1.86 \times 10^{-4}\text{K}^{-1}$ and of oxide cladding as $1 \times 10^{-5}\text{K}^{-1}$ [16].

A standard core thickness of $h = 220$ nm (see Fig. 1) and a fixed input/output waveguide width of $W_1 = 450$ nm were considered for all the designs. Also, using $\Lambda = 220$ nm in the SWG region avoids Bragg effects while guaranteeing a feature size that can be fabricated by conventional e-beam techniques. In order to ensure the mono-mode operation, we limited optimization boundaries of W_2 and W_3 to 350–600 nm and 400–600 nm, respectively. Likewise, we defined the minimum *DC* as 40% and maximum *DC* as 60%.

To enable the comparison of our results with [23], the first step was to find a path length difference ΔL at which the target δL is achieved (i.e., $\delta L = 0.711$ mm and $S \pm 1$ pm/K at the central wavelength). In order to calculate the targeted δL, we used (1), (2) and (4) and found a linear relationship between ΔL and δL for parameters $W_2 = 500$ nm, $W_3 = 500$ nm, DC = 50%. The linear fitting equation is given by (7). Once the targeted δL was achieved, the next step was to calculate the 'common length' L of the waveguide at that particular value of ΔL using (1), (2) and (4). The relationship between ΔL and L is also found to be linear, and the linear fitting equation is given by (8).

$$\delta L = 0.01676\Delta L - 1 \times 10^{-6} \tag{7}$$

$$L = 1.457\Delta L - 2.507 \times 10^{-7} \tag{8}$$

Since the relationship between δL and ΔL and between ΔL and L is linear, therefore, in order to ease the calculations, first gradients ($m_{\delta L \Delta L}$) between δL and ΔL and second gradient ($m_{\Delta L L}$) between ΔL and L, were considered for further calculations. Both gradients are computed for scenarios discussed earlier by sweeping DC between 40% and 60%, W_2 between 350–600 nm, and W_3 between 400–600 nm. The Gradient values $m_{\delta L \Delta L}$ for the parameters DC between 40% and 60%, $W_2 = 500$ nm, and W_3 between 400–600 nm, are shown in Fig. 2(a)–(c), whereas gradient values $m_{\Delta L L}$ for the parameters DC between 40% and 60%, $W_2 = 500$ nm, and W_3 between 400–600 nm, are shown in Fig. 2(d)–(e).

In order to optimize r_{OPD}, we need high $m_{\delta L \Delta L}$ and low $m_{\Delta L L}$ values. Although parameters $m_{\delta L \Delta L}$ and $m_{\Delta L L}$ show similar tendencies, an optimal ratio can be found for larger widths and duty cycles. Given the aforementioned constraints, we have chosen $W_3 = 600$ nm, $W_2 = 600$ nm, and DC = 60%. This leads to the length $L = 50.62$ mm and $\Delta L = 23.56$ mm while still maintaining the value of $\delta L = 0.711$ mm a constant.

Now, by numerically solving (1), (2), and (4) for each wavelength separately, the spectral response of the athermal MZI based on the proposed design is shown in Fig. 3 by a blue-solid line for a 100 nm wavelength range when using an optimal r_{OPD} ($W_3 = 600$ nm, $W_2 = 600$ nm, $DC = 60\%$, $L = 50.62$ mm and $\Delta L = 23.56$ mm). The temperature sensitivity for $L + 0.355$ mm and $L - 0.355$ mm are shown as black-dashed and red-dotted lines, respectively. Our evaluation of the broadband operation of the MZI around the targeted central wavelength $\lambda_0 = 1550$ nm for the maximum allowed deviation of -10 pm/K was found to be from 1500 to 1600 nm. Note, in this particular case, achieving the MZI footprint through r_{OPD} was prioritized over its spectral response flatness (S_{total}). The spectral response flatness can be further optimized and will be discussed in

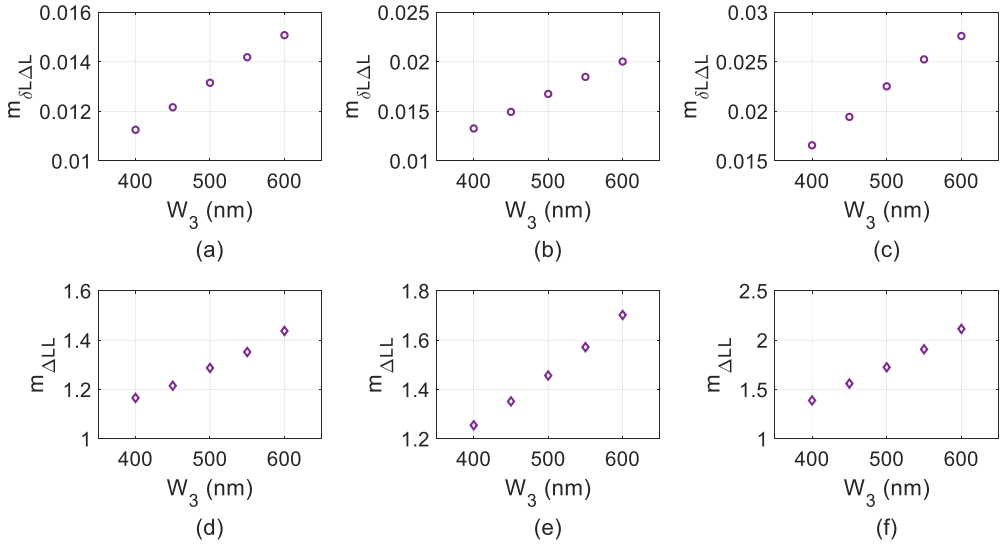

Fig. 2. (a)–(c) Gradient between δL and ΔL for DC = 40%, DC = 50% and DC = 60% for $W_2 = 500$ nm. (d)–(f) Gradient between L and ΔL for subwavelength duty cycles DC = 40%, DC = 50% and DC = 60% for $W_2 = 500$ nm.

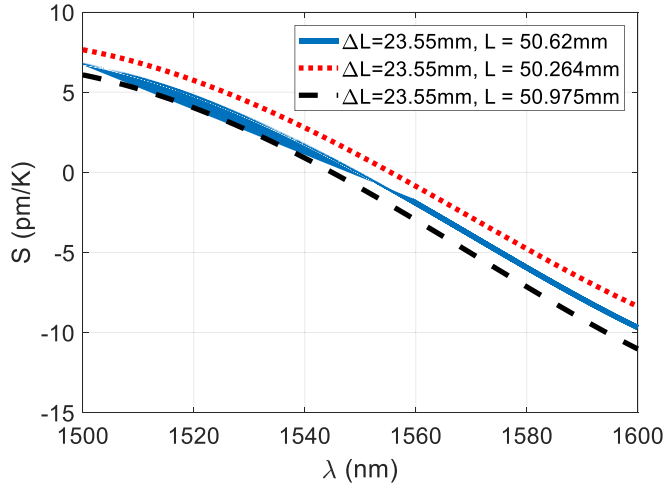

Fig. 3. Temperature insensitivity S of athermal MZI as function of wavelength for $W_2 = 600$ nm, $W_3 = 600$ nm, DC = 60%, $L = 50.62$ mm and $\Delta L = 23.56$ mm is shown in blue solid line. Black dashed and red dotted line shows S for $L + 0.355$ mm and $L - 0.355$ mm, respectively.

Section 5. Note, also spiral waveguides could be used to further reduce the overall device footprint if desired.

For designing any FT microspectrometer, the spectral resolution and FSR plays an important role. The spectral resolution ($\delta\lambda$) and FSR of an FT spectrometer (FSR_{FT}) based on N MZIs is given as:

$$\delta\lambda = \frac{\lambda_0^2}{\left|\Delta L_{\max} n_{g_2} + L\left(n_{g_3} - n_{g_2}\right)\right|} \tag{9}$$

$$FSR_{FT} = \delta\lambda \frac{N}{2}, \tag{10}$$

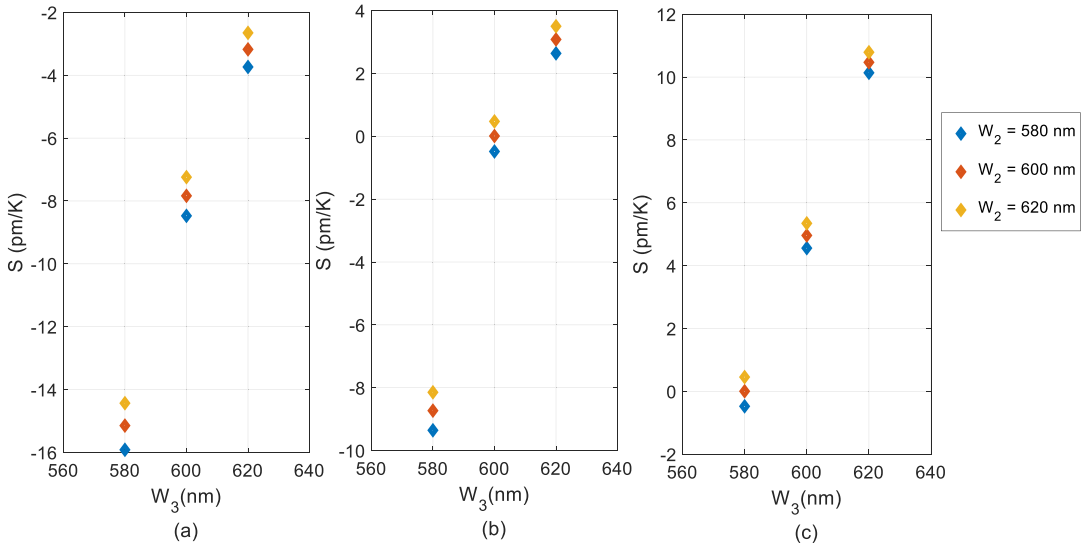

Fig. 4. Temperature sensitivity of the MZI at the central wavelength of 1550 nm as the function of the wire and SWG waveguide width and the SWG duty cycle. (a) 58%. (b) 60%. (c) 62%.

$N = 32$ was used in [1]. $\Delta L_{\max}$ is a maximum path length difference for the MZI, n_{g_2} is a group index of the wire waveguide, and n_{g_3} is a group index of the SWG waveguide. From (9) and (10) one can observe that an FT microspectrometer can be designed for a specific spectral resolution and FSR the application may require. Based on (9) and (10), using $\Delta L_{\max} = 23.56$ mm and $L = 50.62$ mm, we calculated that the spectral resolution and FSR of the FT microspectrometer based on 32 athermal MZIs is 47 pm and 0.76 nm, respectively. Such an athermal device will have its theoretical temperature dependent wavelength shift of 0.01 pm/K for central wavelength of 1550 nm, comparing favorably with [17].

4. Resilience to Fabrication Errors

In order to analyze how fabrication deviations from nominal values may affect the performance of a proposed athermal MZI, we simulated the width variations of its wire and SWG waveguides and duty cycle errors in the SWG region. These effects were first considered independently and then jointly. In particular, we considered variations of ± 20 nm of the width in both waveguides (i.e., W_2 and W_3), and $\pm 2\%$ variations of the duty cycle (DC). Fig. 4 shows the degradation of the temperature sensitivity (S) for W_2 and W_3 ranging between 580 to 620 nm and DC ranging between 58 to 62%. One can see, that variations in W_2 and W_3 values have a significant impact on S (up to -16 pm/K), however this impact can be mitigated by properly selecting the corresponding DC value to generate an opposite effect. Also notice, that the intrinsic high dependence of the SOI platform on fabrication errors is improved by mode delocalization in the SWG region.

5. Bandwidth Enhancement Analyses and Discussion

As mentioned in Section 3, the athermal MZI design was initially optimized for its footprint. However, if more stringent temperature insensitivity limits are required, for example to support applications in a bandwidth region (say, 1500 to 1600 nm), a tradeoff is required between r_{OPD} and S_{total}. Unlike solutions based on wire waveguides of different widths [23], [24], this tradeoff can be achieved by taking advantage of additional degrees of freedom provided by SWG unique properties. This is illustrated in Fig. 5, where the resulting S_{total} over a 100 nm range around 1550 nm is shown as a function of different waveguide parameters: the duty cycle DC between 40% and 60%, W_2 between

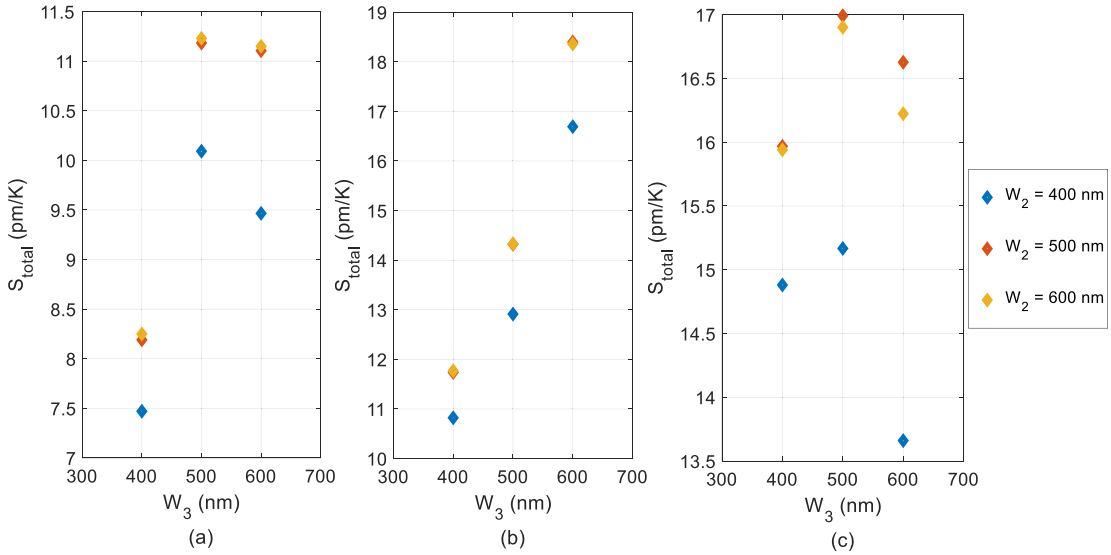

Fig. 5. Overall temperature sensitivity of the athermal MZI in the wavelength range of 1500 to 1600 nm when considering the wire waveguide and SWG waveguide width variations represented by duty cycle. (a) 40%. (b) 50%. (c) 60%.

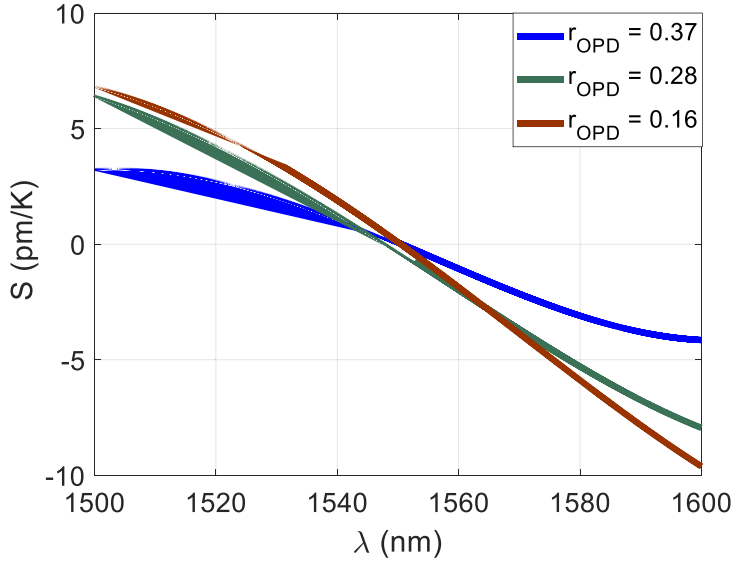

Fig. 6. Illustration of MZI temperature sensitivity in 1550 to 1600 nm wavelength region for relative optical path differences: $r_{OPD} = 0.37$ blue, $r_{OPD} = 0.28$ green and $r_{OPD} = 0.16$ brown.

350–600 nm, and W_3 between 400–600 nm. By analyzing Fig. 5, we found that a smaller waveguide width gives a lower overall temperature sensitivity of the MZI in the 1500 to 1600 nm wavelength range.

Fig. 6 summarizes results related to the MZI temperature sensitivity (S_{total}) in the same 1500 to 1600 nm wavelength region when taking into account different waveguide dimensions and r_{OPD} values:

1) $W_2 = 400$ nm, $W_3 = 400$ nm, DC $= 40\%$, $L = 75.1$ mm, and $\Delta L = 64.4$ mm.
2) $W_2 = 600$ nm, $W_3 = 600$ nm, DC $= 60\%$, $L = 50.6$ mm, and $\Delta L = 23.5$ mm.

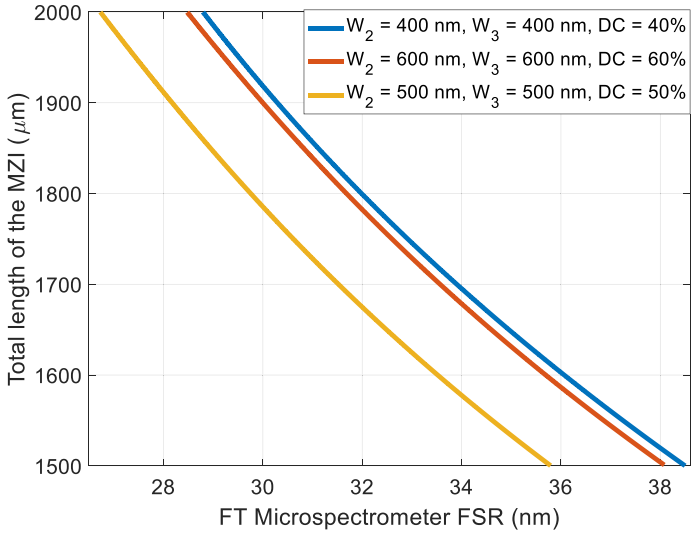

Fig. 7. Illustration of MZI length as function of FT spectrometer FSR for different sets of waveguides dimensions: $W_2 = 400$ nm, $W_3 = 400$ nm, DC $= 40\%$ -blue line; $W_2 = 600$ nm, $W_3 = 600$ nm, DC $= 60\%$ -red line, and $W_2 = 500$ nm, $W_3 = 500$ nm, DC $= 50\%$ -yellow line.

3) $W_2 = 500$ nm, $W_3 = 500$ nm, DC $= 50\%$, $L = 62$ mm, and $\Delta L = 42.5$ mm.

We found that in order to achieve an athermal operation over the range of 100 nm around 1550 nm, one has to select a smaller width of the wire waveguide, and smaller width and DC of the SWG. For this reason, for the proposed athermal MZI design, we selected $W_2 = 400$ nm, $W_3 = 400$ nm, DC $= 40\%$, $L = 75.1$ mm, and $\Delta L = 64.4$ mm. By choosing these values, the S_{total} was found to be 7.5 pm/K. Just for a comparison, this value is less than a one-half of 16.4 pm/K found for the athermal MZI with parameters $W_2 = 600$ nm, $W_3 = 600$ nm, DC $= 60\%$, $L = 50.6$ mm, $\Delta L = 23.5$ mm.

Fig. 7 shows the required total length of the MZI ($L_{total} = L_1 + L_2 + 2 \times L$) in order to achieve its athermal operation as a function of the FT microspectrometer FSR range. Calculations are based on (1), (2), (4), and (10) and waveguides dimensions considered earlier in this section i.e.,:

1) $W_2 = 400$ nm, $W_3 = 400$ nm, DC $= 40\%$.
2) $W_2 = 600$ nm, $W_3 = 600$ nm, DC $= 60\%$.
3) $W_2 = 500$ nm, $W_3 = 500$ nm, DC $= 50\%$.

The study shows that the temperature insensitive MZI can be designing through a combination of SWG and wire waveguides with carefully tailored dimensions. The SWG waveguide adds an additional degree of freedom for controlling the effective refractive index and dispersion through varying the duty cycle (DC). We found that the proposed athermal MZI design is insensitive to changes of the wire and SWG length L up to ± 0.355 mm and the design can be scaled for any FSR and resolution range of FT microspectrometers.

6. Conclusion

We have proposed and analyzed a silicon-on-insulator MZI with an extremely low temperature sensitivity. Temperature compensation is achieved by tailoring SWG properties in one arm of a Mach-Zehnder interferometer. Performance simulations show that by engineering waveguide dimensions, an overall temperature insensitivity below 7.5 pm/K can be attained over a 100 nm range around 1550 nm. The device is insensitive to changes of the wire and SWG length L up to ± 0.355 mm. Errors due to optical path imbalance, their mitigation and the resilience of the athermal design to fabrication errors were then analyzed. We found that trade-offs could be made between the temperature sensitivity, optical path imbalance and fabrication errors by adequately selecting the

SWG length, width, and duty cycle. The proposed athermal MZI design can be applied to interferometer arrays of on-chip Fourier-transform microspectrometers. This will enable a better scalability, wider FSR range and device ability to mitigate challenging environmental influences. This approach sets a new milestone for achieving a better resolution stability in the field of integrated spectroscopy. A spiral waveguide design and reduction of δL will further help with minimizing the device footprint.

References

[1] A. V. Velasco *et al.*, "High-resolution Fourier-transform spectrometer chip with microphotonic silicon spiral waveguides," *Opt. Lett.*, vol. 38, no. 5, pp. 706–708, 2013.
[2] H. Podemore *et al.*, "Demonstration of a compressive-sensing Fourier-transform on-chip spectrometer," *Opt. Lett.*, vol. 42, no. 7, pp. 1440–1443, 2017.
[3] P. R. Griffiths, "The early days of commercial FT-IR spectrometry: A personal perspective," *Appl. Spectrosc.*, vol. 71, no. 3, pp. 329–340, 2017.
[4] M. C. M. M. Souza, A. Grieco, N. C. Frateschi, and Y. Fainman, "Fourier transform spectrometer on silicon with thermo-optic non-linearity and dispersion correction," *Nat. Commun.*, vol. 9, 2018, Art. no. 665.
[5] J. H. Song *et al.*, "Bragg grating-assisted WDM filter for integrated optical triplexer transceivers," *IEEE Photon. Technol. Lett.*, vol. 17, no. 12, pp. 2607–2609, Dec. 2005.
[6] A. Malik *et al.*, "Germanium-on-silicon planar concave grating wavelength (de)multiplexers in the mid-infrared," *Appl. Phys. Lett.*, vol. 103, no. 16, pp. 161119-1–161119-4, 2013.
[7] P. Cheben *et al.*, "A high-resolution silicon-on-insulator arrayed waveguide grating microspectrometer with sub-micrometer aperture waveguides," *Opt. Exp.*, vol. 15, no. 5, pp. 2299–2306, 2007.
[8] J. Huang, J. Yang, H. Zhang, J. Zhang, W. Wu, and S. Chang, "Analysis of tunable flat-top bandpass filters based on graphene," *IEEE Photon. Technol. Lett.*, vol. 28, no. 23, pp. 2677–2680, Dec. 2016.
[9] M. Florjańczyk, P. Cheben, S. Janz, A. Scott, B. Solheim, and D.-X. Xu, "Multiaperture planar waveguide spectrometer formed by arrayed Mach-Zehnder interferometers," *Opt. Exp.*, vol. 15, no. 26, pp. 18176–18189, 2007.
[10] A. V. Velasco, P. Cheben, M. Florjańczyk, and M. L. Calvoa, "Spatial heterodyne Fourier-transform waveguide spectrometers," *Prog. Opt.*, vol. 59, pp. 159–208, 2014.
[11] L. Chrostowski and M. Hochberg, *Silicon Photonics Design*. Cambridge, U.K.: Cambridge Univ. Press, 2015.
[12] P. J. Bock *et al.*, "Subwavelength grating Fourier-transform interferometer array in silicon-on-insulator," *Laser Photon. Rev.*, vol. 7, no. 6, pp. L67–L70, 2013.
[13] M. Nedeljkovic, A. V. Velasco, A. Z. Khokhar, A. Delâge, P. Cheben, and G. Z. Mashanovich, "Mid-infrared silicon-on-insulator Fourier-transform spectrometer chip," *IEEE Photon. Technol. Lett.*, vol. 28, no. 4, pp. 528–531, Feb. 2016.
[14] K. Okamoto, H. Aoyagi, and K. Takada, "Fabrication of Fourier-transform, integrated-optic spatial heterodyne spectrometer on silica-based planar waveguide," *Opt. Lett.*, vol. 35, no. 12, pp. 2103–2105, 2010.
[15] D. M. Kita *et al.*, "High-performance and scalable on-chip digital Fourier transform spectroscopy," *Nat. Commun.*, vol. 9, 2018, Art. no. 4405.
[16] G. Cocorullo and I. Rendina, "Thermo-optical modulation at 1.5 μm in silicon etalon," *Electron. Lett.*, vol. 28, no. 1, pp. 83–85, 1992.
[17] A. Herrero-Bermello *et al.*, "Temperature dependence mitigation in stationary Fourier-transform on-chip spectrometers," *Opt. Lett.*, vol. 42, no. 11, pp. 2239–2242, 2017.
[18] M. M. Milosevic, N. G. Emerson, F. Y. Gardes, X. Chen, A. A. D. T. Adikaari, and G. Z. Mashanovich, "Athermal waveguides for optical communication wavelengths," *Opt. Lett.*, vol. 36, no. 23, pp. 4659–4661, 2011.
[19] J. Teng *et al.*, "Athermal silicon-on-insulator ring resonators by overlaying a polymer cladding on narrowed waveguides," *Opt. Exp.*, vol. 17, no. 17, pp. 14627–14633, 2009.
[20] B. Guha, J. Cardenas, and M. Lipson, "Athermal silicon microring resonators with titanium oxide cladding," *Opt. Exp.*, vol. 21, no. 22, pp. 26557–26563, 2013.
[21] T. Lipka, L. Moldenhauer, J. Müller, and H. K. Trieu, "Athermal and wavelength-trimmable photonic filters based on TiO2-cladded amorphous-SOI," *Opt. Exp.*, vol. 23, no. 15, pp. 20075–20088, 2015.
[22] L. He *et al.*, "Broadband athermal waveguides and resonators for datacom and telecom applications," *Photon. Res.*, vol. 6, no. 11, pp. 987–990, 2018.
[23] B. Guha, A. Gondarenko, and M. Lipson, "Minimizing temperature sensitivity of silicon Mach-Zehnder interferometers," *Opt. Exp.*, vol. 18, no. 3, pp. 1879–1887, 2010.
[24] M. Uenuma and T. Motooka, "Temperature-independent silicon waveguide optical filter," *Opt. Lett.*, vol. 34, no. 5, pp. 599–601, 2009.
[25] J. H. Schmid *et al.*, "Temperature-independent silicon subwavelength grating waveguides," *Opt. Lett.*, vol. 36, no. 11, pp. 2110–2112, 2011.
[26] M. Ibrahim *et al.*, "Athermal silicon waveguides with bridged subwavelength gratings for TE and TM polarizations," *Opt. Exp.*, vol. 20, no. 16, pp. 18356–18361, 2012.
[27] P. J. Bock *et al.*, "Subwavelength grating periodic structures in silicon-on-insulator: A new type of microphotonic waveguide," *Opt. Exp.*, vol. 18, no. 19, pp. 20251–20262, 2010.
[28] P. Cheben, R. Halir, J. H. Schmid, H. A. Atwater, and D. R. Smith, "Subwavelength integrated photonics," *Nature*, vol. 560, pp. 565–572, 2018.
[29] R. Halir *et al.*, "Colorless directional coupler with dispersion engineered sub-wavelength structure," *Opt. Exp.*, vol. 20, no. 12, pp. 13470–13477, 2012.

[30] A. Maese-Novo *et al.*, "Wavelength independent multimode interference coupler," *Opt. Exp.*, vol. 21, pp. 7033–7040, 2013.
[31] D. González-Andrade *et al.*, "Ultra-broadband mode converter and multiplexer based on sub-wavelength structures," *IEEE Photon. J.*, vol. 10, no. 2, Apr. 2018, Art. no. 2201010.
[32] Z. Cheng and H. K. Tsang, "Experimental demonstration of polarization-insensitive air-cladding grating couplers for silicon-on-insulator waveguides," *Opt. Lett.* vol. 39, no. 7, pp. 2206–2209, 2014.
[33] J. M. Luque-González *et al.*, "Tilted subwavelength gratings: Controlling anisotropy in metamaterial nanophotonic waveguides," *Opt. Lett.*, vol. 43, no. 19, pp. 4691–4694, 2018.
[34] T. Shoji, T. Tsuchizawa, T. Watanabe, K. Yamada, and H. Morita, "Low loss mode size converter from 0.3 μm square Si wire waveguides to single mode fibres," *Electron. Lett.*, vol. 38, no. 25, pp. 1669–1670, 2002.
[35] Y. Fu, T. Ye, W. Tang, and T. Chu, "Efficient adiabatic silicon-on-insulator waveguide taper," *Photon. Res.*, vol. 2, no. 3, pp. A41–A44, 2014.
[36] [Online]. Available: https://www.lumerical.com/products/fdtd/
[37] J. G. Wangüemert-Pérez *et al.*, "Evanescent field waveguide sensing with subwavelength grating structures in silicon-on-insulator," *Opt. Lett.*, vol. 39, no. 15, pp. 4442–4445, 2014.
[38] [Online]. Available: https://www.lumerical.com/learn/video/swg-bandstructures/